CLIMATOLOGY

Vegetation feedbacks accelerated the late Miocene climate transition

Ran Zhang[1,2]*, Jiaqi Guo[3], Catherine D. Bradshaw[4,5], Xiyan Xu[1], Tiantian Shen[6], Shufeng Li[7], Junsheng Nie[6], Chunxia Zhang[8], Xiangyu Li[9], Ze Liu[10], Jian Zhang[3], Dabang Jiang[1], Yongyun Hu[3], Jimin Sun[8,11]*

The late Miocene was an important stage for the formation of modern-like ecological and environmental patterns. Proxy data from the middle to late Miocene reveal that large-scale cooling and drying occurred; however, the reasons for this climate transition remain unclear. Through a compilation of proxy data and climate simulations, our results indicate that atmospheric CO_2 decline markedly decreased the temperature and reduced the precipitation in most of the land area, while the paleogeographic changes enhanced cooling at northern high latitudes and increased precipitation in East Asia, East Africa, and South America. In comparison, vegetation changes accelerated cooling at northern high latitudes (the maximum cooling exceeded 10°C) and modulated precipitation at low- and mid-latitude continents (the maximum decrease was close to 30%). This deepens the understanding of the mechanism of the late Miocene climate transition and highlights the importance of vegetation feedbacks during global climate change.

INTRODUCTION

The late Miocene [11.6 to 5.3 million years (Ma)] represents an important period in Earth's history, in which global warmth and a reduced equator-to-pole temperature gradient experienced during the middle Miocene shifted to near-modern biogeographical and climatic conditions (*1*–*3*). Reconstructions show that from the middle to late Miocene, atmospheric CO_2 concentrations decreased (Fig. 1B), with notable cooling occurring at higher latitudes (Fig. 1, A and C). Meanwhile, the tectonic movements, including the uplifting of the central Asian orogenic belt and northern Tibetan Plateau (*4*–*6*), Rocky Mountains (*7*), Andes (*8*), mountains in eastern Africa (*9*), and Alps (*10*), were extraordinarily active during the late Miocene. The continental climate patterns and ecosystems also changed markedly (*11*, *12*), such as the expansion of the steppe zone (Fig. 1, D and E) (*13*) and a transition in the mammalian dietary habits toward increasing consumption of C_4 plants (Fig. 1F) (*14*). Various proxies across regions have demonstrated that the global climate dried during the late Miocene (Fig. 1, G to K), which was accompanied by increased terrestrial sedimentation rates (*15*), eolian grain sizes and erosion rates (*16*), and oceanic dust fluxes (*17*).

It is widely recognized that both atmospheric CO_2 decline and paleogeographic change drove the climate and ecological shifts during the late Miocene, yet their relative contributions remain contentious. Some scholars have argued that paleogeographic changes were primarily responsible for the evolution of the regional climate in the late Miocene, with minor contributions from atmospheric CO_2 (*18*–*20*). Others have demonstrated that decreased atmospheric CO_2 was the key driver of late Miocene cooling and drying (*21*, *22*). The contributions of paleogeography and atmospheric CO_2 varied regionally. For example, aridification in central Asia throughout the middle to late Miocene was influenced mainly by the uplift of the Tibetan Plateau, whereas drying in the rest of Asia and Europe was driven by the decrease in atmospheric CO_2 (*23*). Continuous decreases in temperature and precipitation during the middle to late Miocene were detected in different regions, which cannot be solely attributed to paleogeographic changes. In contrast, decreases in atmospheric CO_2 can leave a simultaneous imprint on different regions, but the responses of climate and ecological environments across regions lag behind the changes in atmospheric CO_2 and have certain differences (Fig. 1). Therefore, neither paleogeography nor atmospheric CO_2 fully explained the global climate transition during the late Miocene.

Vegetation changes have been considered important factors affecting the past climate (*24*–*27*). During the late Miocene, one of the most pivotal events was the transition from C_3 to C_4 vegetation (Fig. 1, D and E), which showed slight temporal variations across continents (*28*–*31*). The reconstructed vegetation distribution indicates that broadleaf trees decreased in Europe, Asia, North America, and Australia and that shrubs and grasses expanded in central Asia, North Africa, North America, and Australia from the middle to late Miocene (fig. S1 and table S1) (*3*, *32*). Moreover, the limited data in Arctic regions seem to support a southward shift of needleleaf trees (fig. S1) (*3*, *32*). A recent study also demonstrated that the initiation and diversification of the Arctic flora occurred starting in the early late Miocene, accompanied by an increasingly open Arctic forest canopy and an increase in shrubs and herbs (*33*). Large-scale ecosystem transformation may have had an important impact on the global climate; however, how vegetation feedbacks to climate and its role in the middle to late Miocene climate transition remain unknown.

[1]State Key Laboratory of Earth System Numerical Modeling and Application, Institute of Atmospheric Physics, Chinese Academy of Sciences, Beijing, China. [2]Collaborative Innovation Center on Forecast and Evaluation of Meteorological Disasters (CIC-FEMD), Nanjing University of Information Science and Technology, Nanjing, China. [3]Department of Atmosphere and Ocean Sciences, School of Physics, Peking University, Beijing, China. [4]The Global Systems Institute, University of Exeter, Exeter, UK. [5]Met Office Hadley Centre, Exeter, UK. [6]College of Earth and Environmental Science, Lanzhou University, Lanzhou, China. [7]CAS Key Laboratory of Tropical Forest Ecology, Xishuangbanna Tropical Botanical Garden, Chinese Academy of Sciences, Mengla, China. [8]Institute of Geology and Geophysics, Chinese Academy of Sciences, Beijing, China. [9]Department of Atmospheric Science, School of Environmental Studies, China University of Geosciences, Wuhan, China. [10]Frontiers Science Center for Deep Ocean Multispheres and Earth System, Key Lab of Submarine Geosciences and Prospecting Techniques, MOE and College of Marine Geosciences, Ocean University of China, Qingdao, China. [11]University of Chinese Academy of Sciences, Beijing, China.
*Corresponding author. Email: zhangran@mail.iap.ac.cn (R.Z.); jmsun@mail.iggcas.ac.cn (J.S.)

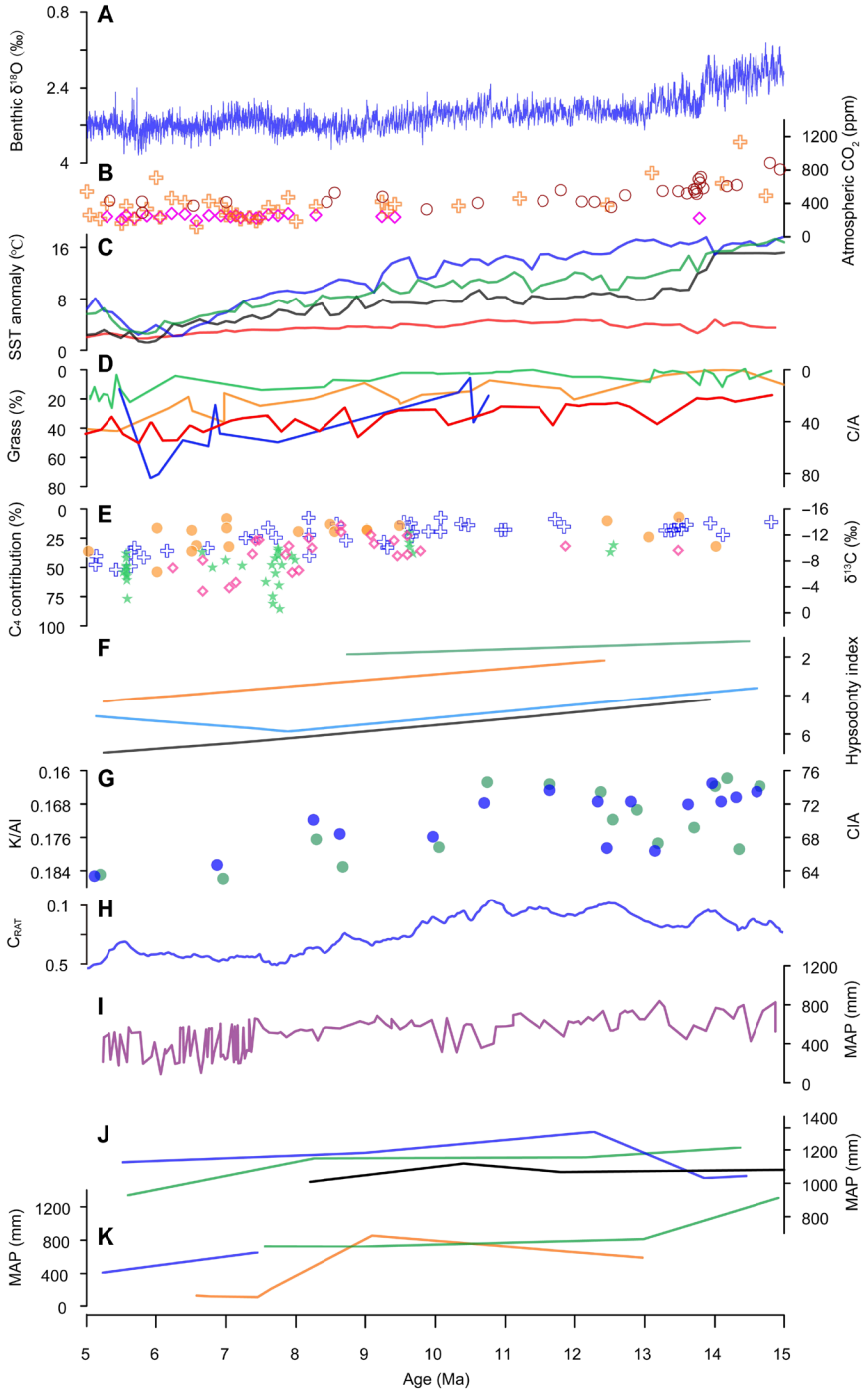

Fig. 1. Climatic, vegetation, and animal records from 15 to 5 Ma. (**A**) Benthic foraminifera $\delta^{18}O$ (*2*). (**B**) Atmospheric CO_2 reconstructions from boron isotopes (circle) and alkenones (cross and diamond) (*36*). (**C**) Regionally averaged sea surface temperature (SST) anomalies (*66*) for the tropics (red), Northern Hemisphere mid-latitudes (black), Northern Hemisphere high latitudes (blue), and Southern Hemisphere (green). (**D**) Grass proportions for North America (orange) (*39*), South America (green) (*68*), and central Asia (red) (*69*) and the Chenopodiaceae/Amaranthaceae (C/A) of East Africa (blue) (*41*). (**E**) C_4 plants for North America (orange) (*70*) and West Africa (blue) (*28*) and $\delta^{13}C$ of sediments and mammals for South America (green) and South Asia (pink) (*71*). (**F**) Hypsodonty trends for equids (black), antilocaprids (blue), camelids (orange), and dromomerycids (green) in North America (*14*). (**G**) K/Al ratio (green) and chemical index of alteration (CIA) (blue) from Indus Marine A-1 (*72*). (**H**) The ratio of chlorite/(chlorite + haematite + goethite) (C_{RAT}) from Ocean Drilling Program site 1148 (*72*). (**I**) Quantitative mean annual precipitation (MAP) reconstruction in the northeastern Tibetan Plateau using the average of three methods (weighted averaging partial least squares, modern-analog technique, and random forest) (*73*). (**J**) Quantitative MAP reconstruction using the coexistence approach (CA) for Ukraine (green) and Serbia (blue) (*51*, *74*) and the average of three methods (climate reconstruction software, climate reconstruction analysis, and the CA) for UK (black) (*75*). (**K**) Quantitative MAP reconstruction using transfer functions based on the percent grazing species (blue), percent Macropodidae (green), and percent mammals in the size range of 45 to 180 kg (orange) for Australia (*55*). ‰, per mil; ppm, parts per million.

Overall, previous modeling studies have generally demonstrated that atmospheric CO_2 decline and paleogeographic change are the main factors influencing the late Miocene climate transition, but most have not separated the role of vegetation feedbacks (*18*–*20*). Here, through the integration of proxy data and seven global climate simulations with the Community Earth System Model (CESM) 1.2.2 based on middle Miocene (~14 Ma) and late Miocene (~6 Ma) paleogeographies (*34*), we provide important insights into the predominant mechanism for the late Miocene climate transition demonstrating our hypothesis that vegetation feedback was also an important factor that accelerated the late Miocene climate transition. In particular, we used a synthesis of Miocene sea surface temperature (SST) and terrestrial annual temperature (TAT) data (table S2) (*35*) and collected precipitation reconstructions with 121 qualitative and 96 quantitative data points derived from the literature (table S3) to compare the climate conditions in the middle and late Miocene. In addition, we conducted global climate simulations (Table 1) to isolate the individual effects of atmospheric CO_2 decline, paleogeographic change, and vegetation feedbacks on the climate transition from the middle to late Miocene.

RESULTS AND DISCUSSION

Climate transition from the middle to late Miocene

According to global temperature and regional SST records (Fig. 1) (*1*, *2*), the overall trend from the middle to late Miocene was cooling, in parallel with decreasing atmospheric CO_2 (*36*, *37*). The SST records indicate a consistent cooling pattern, with more pronounced cooling occurring at high latitudes in the Northern Hemisphere than in the Southern Hemisphere (Fig. 2A). The TAT records also show marked cooling at northern high latitudes (Fig. 2B). The model results (LM280veg − MM700veg) indicate that the climate cooled from the middle to late Miocene, with clear regional differences. The simulated annual surface air temperature (SAT) decreased in most land areas, with larger magnitudes observed at high latitudes (Fig. 2C). Similarly, the simulated SSTs also decreased, particularly in the northern parts of the Pacific and Atlantic (fig. S2A). Overall, the reconstructed cooling from the middle to late Miocene is captured reasonably well by the simulations, particularly the greater cooling documented at northern high latitudes.

Precipitation reconstructions reveal that the large-scale climate became drier from the middle to late Miocene. This drying trend is notable in Europe, central Asia, western North America, and Australia, but there are also regional wetting trends, such as in some regions in East Asia, East Africa, and South America (Fig. 2D). The model results (LM280veg − MM700veg) reproduce the decreasing annual precipitation in most land areas, especially at northern mid- to high latitudes, North Africa, northern South America, and South Australia (Fig. 2D). Although limited records exist, the wetting trends in the northeastern Tibetan Plateau, East Africa, and southern South America are also reproduced by the simulations (Fig. 2D). In addition, the simulated surface runoff and soil moisture reveal obvious hydrological changes and direct effects of precipitation, particularly at low- and mid-latitude continents (fig. S3).

Climate change is also reflected in other aspects of the climate system. From the middle to late Miocene, the meridional temperature gradient increased because of the disproportionately greater cooling experienced at the poles. As a result, the mid-latitude westerlies in the Northern Hemisphere strengthened according to thermal wind theory (*38*), and the intertropical convergence zone migrated southward, especially in North Africa and the Pacific (fig. S4). The regional hydrologic cycle weakened; in particular, the monsoon domain shrunk in North Africa, northwestern East Asia, and southern Australia (fig. S4), accompanied by a weakened summer monsoon and increased regional dryland aridity. In contrast, the monsoon domain expanded in the Arabian Peninsula, Tibetan Plateau, and northwestern Australia due to the increased land area or height. These results are consistent with the expansion of grasslands in North America (*39*), central Asia (*40*), Africa (*41*), and Australia (*42*); the expansion of deserts in Africa (*43*) and Asia (*44*); and the weakening of Asian and North African monsoons (*43*, *45*). Overall, multiple aspects of the climate system markedly changed via atmospheric circulation and ocean-atmosphere interactions.

Vegetation feedbacks enhance cooling and drying

As demonstrated in our sensitivity experiments, the atmospheric CO_2 decline markedly decreased the global temperature and large-scale

Table 1. Information about the spin-up of Miocene simulations. Deep ocean temperatures are averaged between 2649 and 4126 m. The temperature trend is calculated as the average of the final 100 years of the simulation minus the 100 years before that simulation to obtain a trend per century. The prescribed vegetation is from the proxy-based reconstruction of the Tortonian.

Experiment	Paleogeography	Antarctic ice sheet	CO_2 (ppmv)	Vegetation	Integration (year)	TOA radiation imbalance (W m^{-2})	SAT (°C)	SAT trend (°C/century)	Deep ocean temperature trend (°C/century)
MM700	14 Ma	Approximately half	700	Prescribed	2200	0.03	19.77	−0.01	−0.01
MM700veg	14 Ma		700	Simulated	600	0.03	19.65	−0.01	0.00
MM280	14 Ma		280	Prescribed	2200	−0.02	16.23	−0.03	−0.01
MM280veg	14 Ma		280	Simulated	600	−0.00	16.11	0.01	0.01
LM280	6 Ma	Full	280	Prescribed	2500	0.05	15.99	−0.02	0.01
LM280veg	6 Ma		280	Simulated	600	−0.06	15.50	0.00	−0.01
MM280_LMtopo	14-Ma Paleogeography and 6-Ma topography	6 Ma	280	Prescribed	500	0.03	16.24	0.01	0.00

precipitation (Fig. 3, A and B). The model results (MM280 − MM700) show more pronounced cooling at high latitudes (Fig. 3A), which is consistent with the records (Fig. 2). However, the reconstructed SSTs showing greater cooling at northern high latitudes than at southern high latitudes (Fig. 2A) could not be reproduced by simulation driven by a decline in atmospheric CO_2 (Fig. 3A). In addition, the decrease in atmospheric CO_2 generally decreased large-scale precipitation through the weakened hydrologic cycle (Fig. 3B), which is consistent with previous modeling studies (*25*, *35*), but the reconstructed regional increased precipitation over East Asia, East Africa, and South America (Fig. 2D) was not captured by the simulation (Fig. 3B). These discrepancies suggest that additional forcing factors beyond the atmospheric CO_2 decline are needed to explain the climate transition during the late Miocene.

Our simulations revealed that the paleogeographic changes experienced from the middle to late Miocene further modulated the temperature and precipitation changes. Paleogeographic changes (LM280 − MM280) led to marked cooling at northern high latitudes and in the Antarctic, with greater cooling at northern high latitudes (Fig. 3C). The precipitation also decreased at northern mid- to high latitudes owing to the weakened hydrologic cycle and in North Africa due to the closure of the Tethyan seaway via the weakening of the African summer monsoon (*43*). In addition, the precipitation increased on the Tibetan Plateau, East Africa, and northern Australia due to increases in elevation (fig. S5) by strengthening the water vapor convergence (Fig. 3D). This finding was further confirmed by a sensitivity experiment of the topographic changes from the middle to late Miocene based on the middle Miocene boundary conditions (fig. S6). Thus, by incorporating the paleogeographic changes and the atmospheric CO_2 changes, the simulated patterns of temperature and precipitation are more consistent with the records (Fig. 2), particularly the greater cooling seen at northern high latitudes and increased precipitation in the northeastern Tibetan Plateau, East Africa, and southern South America.

In response to the colder and drier climate from the middle to late Miocene, the simulated vegetation underwent notable changes. The main features included a southward shift in needleleaf trees at northern high latitudes; a decrease in broadleaf trees in Europe, Asia, North Africa, North America, and Australia; and an expansion of shrubs and grasses (fig. S7). This result is broadly consistent with the reconstruction (fig. S1 and table S1). Our simulations revealed that these vegetation changes also caused feedbacks to climate that further affected the temperature and precipitation changes (Fig. 3, E and F).

We find that vegetation feedbacks [(LM280veg − MM700veg) − (LM280 − MM700)] markedly accelerated northern high-latitude cooling and modulated low- and mid-latitude continental hydrological climate (Fig. 3, E and F). The globally averaged SAT cooling due to vegetation feedbacks was −0.37°C, which was clearly lower than the cooling (−3.54°C) caused by the atmospheric CO_2 decline but greater than the cooling (−0.24°C) caused by the paleogeographic change. Vegetation feedbacks also caused the globally land-averaged precipitation to decrease by −0.08 mm/day, which was

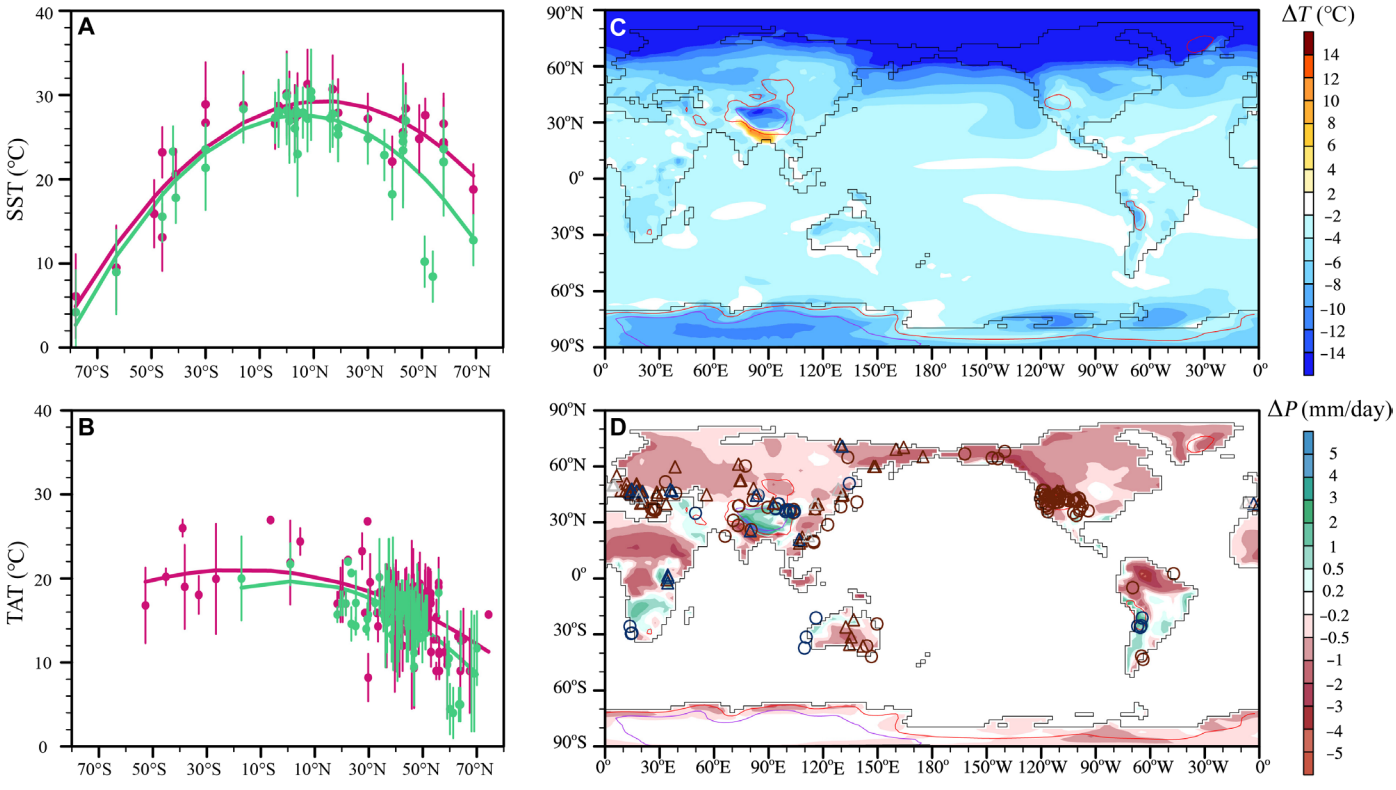

Fig. 2. Temperature and precipitation anomalies from the middle to late Miocene. Average zonal (**A**) SST and (**B**) TAT computed from the proxy (dots) for the middle (red) and late (green) Miocene (*35*). The thick green (red) line is the overall trend and represents the average zonal temperature estimate. The simulated annual (**C**) SAT and (**D**) precipitation anomalies are due to combined paleogeographic change and atmospheric CO_2 decline with dynamic vegetation (LM280veg − MM700veg). In (D), qualitative (circle) and quantitative (triangle) proxy data are displayed as wetter (blue), drier (red), and no change (gray) at the 6-Ma location according to the global plate model (*76*). Elevations equal to 1500 and 3000 m in LM280veg are highlighted with red and purple contours.

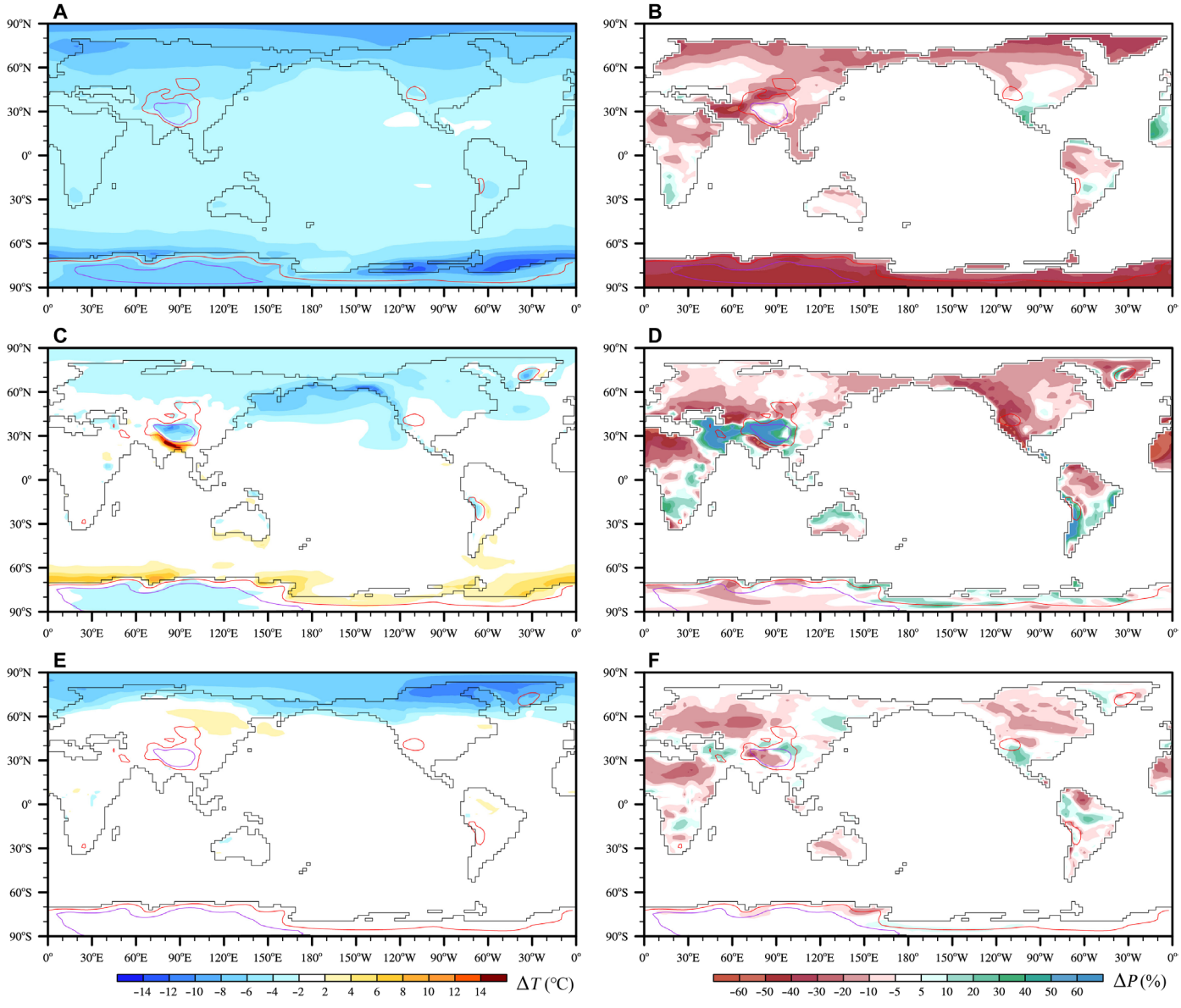

Fig. 3. Temperature and precipitation anomalies due to individual factors. The simulated annual SAT anomalies (left) and precipitation changes (divided by precipitation from MM700veg) (right) due to (**A** and **B**) atmospheric CO_2 decline with static prescribed vegetation (MM280 − MM700); (**C** and **D**) paleogeographic change with static prescribed vegetation (LM280 − MM280); and (**E** and **F**) vegetation feedback response to combined effects of paleogeographic change and atmospheric CO_2 decline [(LM280veg − MM700veg) − (LM280 − MM700)].

lower than the decreases of −0.27 and −0.12 mm/day caused by the atmospheric CO_2 decline and paleogeographic change, respectively. However, the corresponding effect was more pronounced regionally. Owing to vegetation feedbacks, precipitation largely decreased in mid-latitude Europe and North America, North Africa, Australia, and northern South America and increased in East Asia, South Africa, and northeastern South America (Fig. 3F). For example, in North Africa, the maximum precipitation decrease was close to 30%, which was comparable to the decrease in response to atmospheric CO_2 decline. Moreover, the maximum cooling experienced at northern high latitudes due to vegetation feedbacks exceeded 10°C (Fig. 3E), which was a greater decrease than the respective effects from atmospheric CO_2 and paleogeography (Figs. 3 and 4). By comparing the SST changes from the middle to late Miocene, the model results with vegetation feedbacks better fit the SST records, with a higher correlation found between the trends of the SST changes in the records and the model results when vegetation feedbacks are included (fig. S8).

Mechanisms for vegetation feedbacks to climate

The enhanced northern high-latitude cooling due to vegetation feedbacks is related to direct vegetation-driven surface albedo changes and indirect water vapor, cloud, and sea ice feedbacks (Fig. 5). The surface albedo increased largely at northern high latitudes after the vegetation changed (fig. S9). This occurred because the surface albedo of shrubs and grasses is greater than that of needleleaf trees and

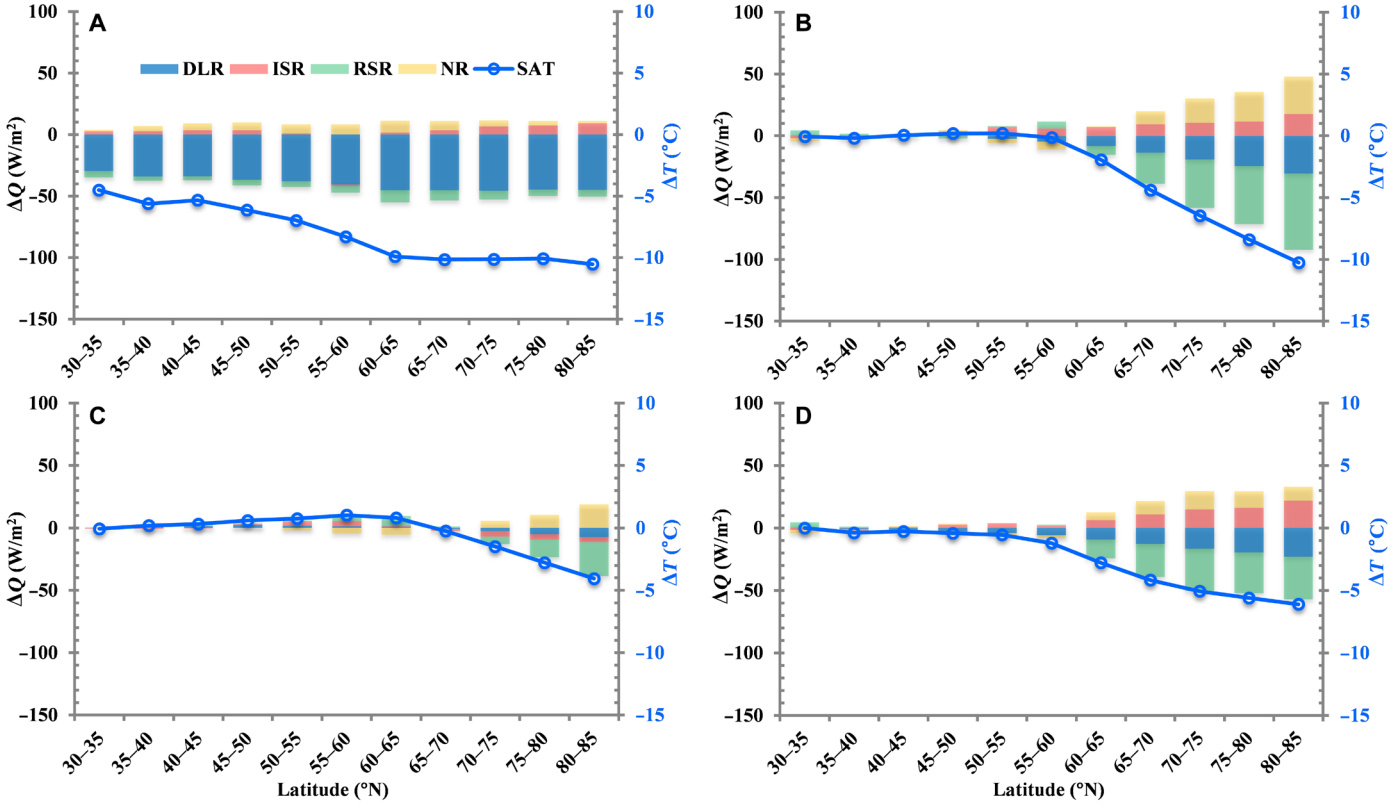

Fig. 4. Latitudinally averaged radiation and SAT anomalies. The latitudinally averaged distributions of annual anomalies at the 5° scale in downwelling longwave radiation (DLR), incident solar radiation (ISR), reflected solar radiation (−RSR), surface net radiation (−NR; including sensible heat flux, latent heat flux, and ground heat flux), and SAT due to (**A**) combined paleogeographic change and atmospheric CO_2 decline with static prescribed vegetation (LM280 − MM700); vegetation feedback response to (**B**) combined effects of paleogeographic change and atmospheric CO_2 decline [(LM280veg − MM700veg) − (LM280 − MM700)], (**C**) atmospheric CO_2 decline [(MM280veg − MM700veg) − (MM280 − MM700)], and (**D**) paleogeographic change [(LM280veg − MM280veg) − (LM280 − MM280)].

increases further after being covered by snow. Geological evidence suggests that, in the northern regions of Canada and Alaska, the ratio of shrubs and herbaceous plants to trees increased, resulting in a more open forest canopy (*33*), supporting an increase in surface albedo at northern high latitudes. As a result, the reflected solar radiation (RSR) largely increased (Fig. 4). The expansion of grasses and shrubs in place of needleleaf trees at northern high latitudes also reduced the latent heat flux and atmospheric water vapor content owing to the decreased evapotranspiration (ET) (fig. S10). The reduced ET and atmospheric water vapor content decreased the cloud cover, resulting in positive shortwave cloud forcing and negative longwave cloud forcing at northern high latitudes, which increased incident solar radiation (ISR) and attenuated downwelling longwave radiation (DLR) (Fig. 4). Moreover, the altered vegetation weakened the sensible and latent heat fluxes, reflecting the decreased surface net radiation (NR) (Fig. 4). As a result, in northern high-latitude land areas, the increased RSR and decreased DLR outweighed the effects of increased ISR and decreased NR, ultimately leading to cooling in this region (Fig. 4B). Cooling also occurred in the adjacent ocean due to air mass transfer and was further amplified through water vapor, cloud, and sea ice feedbacks. In addition to cooling, warming occurred in northeastern Eurasia due to vegetation feedbacks (Fig. 3E), primarily resulting from the decreased RSR related to the reduced surface albedo caused by the southward shift of needleleaf trees (fig. S9).

When we compare our dynamic vegetation simulations for paleogeographic change and atmospheric CO_2 decline, we find that vegetation feedbacks due to paleogeographic change [(LM280veg − MM280veg) − (LM280 − MM280)] induced more cooling at northern high latitudes than did the vegetation feedbacks due to atmospheric CO_2 decline [(MM280veg − MM700veg) − (MM280 − MM700)] (Fig. 4, C versus D). Owing to large-scale cooling and drying forced by atmospheric CO_2 decline (Fig. 3, A and B), there was a southward shift in needleleaf trees at northern high latitudes and a decrease in broadleaf trees at northern middle latitudes (fig. S7). As a result of these changes in vegetation and surface albedo, the RSR increased and, in turn, caused the cooling experienced at northern high latitudes (Fig. 4C). In comparison, the vegetation feedbacks due to paleogeographic change induced more cooling at northern high latitudes, which was related not only to the increased RSR (Fig. 4D) caused by the increased surface albedo but also to the decreased DLR (Fig. 4D) driven by the decreased longwave cloud forcing.

Why did a change in paleogeography lead to the southward migration of needleleaf trees at northern high latitudes? The paleogeographic changes used as model boundary conditions included changes in topography and seaways. The increased topographic height resulted in regional cooling due to the effects of the temperature lapse rate, such as that in the Tibetan Plateau and Antarctic (fig. S6). However, this cooling was not widespread at northern high latitudes. Thus, cooling at northern high latitudes was not determined by changes in the topography. We found that the simulated SSTs driven by paleogeography

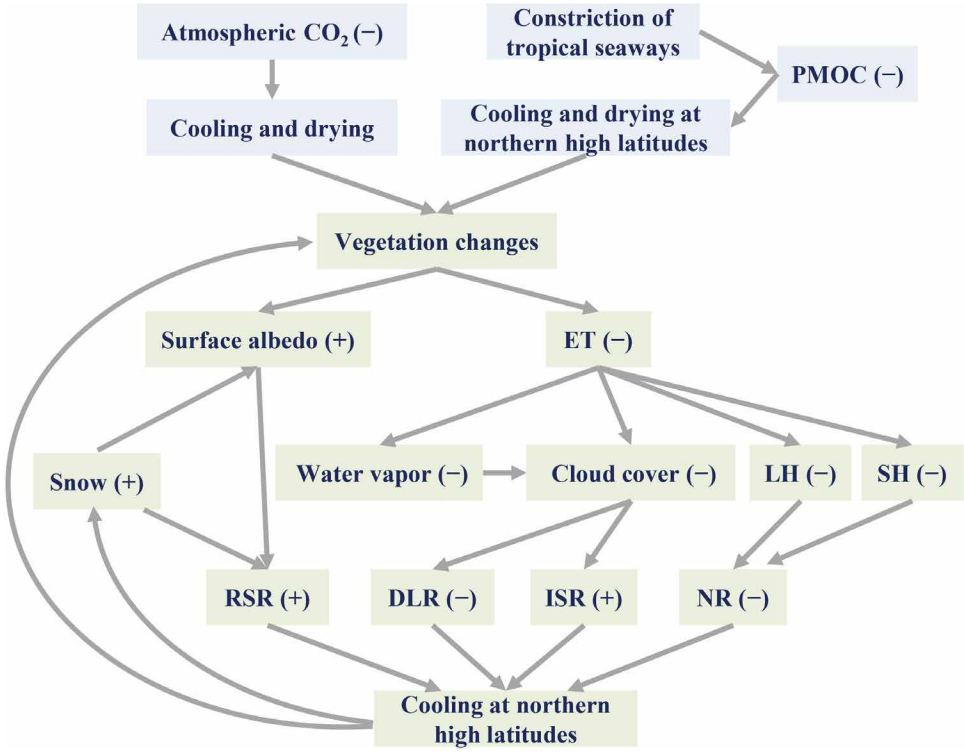

Fig. 5. Schematic diagram of the effects of vegetation feedbacks at northern high latitudes. Vegetation feedbacks enhanced northern high-latitude cooling through direct vegetation-driven surface albedo changes and indirect water vapor and cloud radiative feedbacks. The symbols + and − denote the increase and decrease in the variables, respectively. PMOC, Pacific meridional overturning circulation; ET, evapotranspiration; LH, latent heat; SH, sensible heat; RSR, reflected solar radiation; DLR, downwelling longwave radiation; ISR, incident solar radiation; NR, net radiation.

generally decreased in most of the Northern Hemisphere but increased in the Southern Hemisphere (fig. S2B), demonstrating that ocean surface heat decreased in the Northern Hemisphere but increased in the Southern Hemisphere.

These SST changes caused by paleogeography were closely related to the varied ocean circulation. In the middle Miocene, the simulated Pacific meridional overturning circulation (PMOC) was strong, and the Atlantic meridional overturning circulation (AMOC) was weak (fig. S11). In comparison, the PMOC was largely reduced, and the AMOC developed instead in the late Miocene (fig. S11). In LM280 compared to MM280, the deep convection was intensified in the Southern Ocean while reduced in the North Pacific (fig. S12). These simulated AMOC and PMOC from the middle to late Miocene seem consistent with geological records, particularly a developing stage of the AMOC during the late Miocene (12 to 9 Ma) (*46*, *47*) and a possible weak state of the PMOC during the middle Miocene compared with the nonexistent state during the late Miocene (*46*). The boundary conditions considered here from the middle to late Miocene included changes in paleogeography, atmospheric CO_2, and the Antarctic ice sheet. Our simulations indicate that the weakened PMOC from the middle to late Miocene was due mainly to changes in paleogeography rather than a decrease in atmospheric CO_2 (fig. S11). The sensitivity experiment of the changed topography and Antarctic ice sheet also revealed slight changes in the PMOC and AMOC (fig. S11), thereby implying the important impacts of interocean gateways on modulating the meridional overturning circulation. Moreover, the changed interocean gateways mainly occurred at low latitudes (*34*), including the closure of the Tethyan seaway and the constriction of the Central American Seaway (CAS) and the Indonesian seaway. Previous modeling studies tend to agree that a strong AMOC does not exist with open tropical seaways (*48*, *49*), but the PMOC possibly dominates (*50*). Brierley and Fedorov (*49*) reported that the closure of the CAS strengthened the AMOC. Tan *et al.* (*50*) recently reported that the combined opening of the CAS and Indonesian seaways can generate an active PMOC. Thus, the constriction of these tropical seaways from the middle to late Miocene may have weakened the PMOC, which led to the southward migration of needleleaf trees through cooling and accompanied drying at northern high latitudes. Note that the weakened PMOC during the late Miocene is rarely observed in previous Miocene climate modeling perhaps because of the difference in the boundary conditions used compared to those in our study. We used recently reconstructed paleogeographies for the middle Miocene (~14 Ma) and late Miocene (~6 Ma) (*34*), and, therefore, this result remains to be verified by other models with the same boundary conditions.

In addition to temperature changes, vegetation feedbacks due to paleogeographic change also generally contributed more to precipitation changes than did the vegetation feedbacks due to atmospheric CO_2 decline (fig. S13). We further decomposed the physical processes that controlled precipitation changes due to vegetation feedbacks using the moisture budget equation. In most regions with distinct changes in precipitation due to vegetation feedbacks, the dynamic component of vertical moisture advection generally contributed more to precipitation changes. The exception was North

America, in which the thermodynamic component of horizontal moisture advection contributed more to the changes in precipitation. At low- and mid-latitude continents, changes in atmospheric circulation, rather than evaporation and atmospheric water vapor content, generally dominated the changes in precipitation induced by vegetation feedbacks.

Our study emphasizes the climate effects from paleogeographic changes and vegetation feedbacks during the late Miocene. In addition to the decline in atmospheric CO_2, the climate at northern high latitudes could have been distinctly affected by paleogeographic changes through varied ocean circulation. Moreover, vegetation feedbacks accelerated cooling at northern high latitudes, which was even comparable to the combined effects of the atmospheric CO_2 decline and paleogeographic change. The effect of vegetation feedbacks thus cannot be ignored. Therefore, paleogeographic change and vegetation feedbacks were likely important factors for cooling at northern high latitudes during the late Miocene, providing additional important mechanisms to constrain the cold environment at northern high latitudes and promote the beginning of ice sheet formation in Greenland.

Using a compilation of proxy data and model results, the climate from the middle to late Miocene and the underlying mechanism were investigated here in detail. Our results distinguished the distinct effects from the atmospheric CO_2 decline, paleogeographic change, and vegetation feedbacks. Previously overlooked vegetation feedbacks were an important factor that accelerated the late Miocene climate transition. Note that uncertainties remain in the paleogeography used, especially the depths of major seaways, paleobathymetry, and land-sea distribution surrounding the Arctic and paleoaltimetric reconstructions in high-elevation regions (*34*). Although uncertainties remain, both our model results and geological records reveal greater cooling at northern high latitudes and large-scale drying climates with some regional wet trends. Our model results were generally consistent with those of previous modeling studies, including Miocene global warmth (*25*, *35*), regional (such as Asia and North Africa) climate evolution during the late Miocene (*20*, *43*), and effects from vegetation changes on northern high-latitude temperatures and low- and mid-latitude continental hydrological cycles (*24*, *25*, *27*). These qualitative consistencies support our conclusions.

MATERIALS AND METHODS

Data

We collect global precipitation data with 121 qualitative data points and 96 quantitative data points derived from the literature (table S3). The data are partly available from the PANGAEA database (*51*), the National Oceanic and Atmospheric Administration paleoclimatology database (*52*), and other synthesized data (*23*). Many quantitative precipitation data come from the coexistence approach, which is based on the nearest living relative method. This approach relies on the close relationship between modern and fossil plants, assuming that fossil taxa have similar climatic requirements to very close living relatives, making it suitable for reconstructing pre-Quaternary climates, as pre-Quaternary plant species may differ from modern ones (*53*). We also collect data via the transfer function approach for paleosols (*54*) and fossil mammalian fauna (*55*). In comparison, qualitative data predominantly consist of various effective moisture proxies, including the chemical index of alteration from sediments, $\delta^{18}O$ values from soil carbonate, magnetic susceptibility of loess, and pollen indicators for vegetation changes (*23*).

To accurately determine the average hydroclimate signal, priority is given to data with a longer time span of the middle and late Miocene. Data with shorter time spans (e.g., less than 1 Ma) are excluded to minimize the effects of climate variability over a smaller timescale. Specifically, quantitative data primarily originate from reliable databases or synthesis datasets, whereas qualitative data are derived from individual sampling points or integrated climate curves across multiple points within a region. Integrated climate curves include at least three reliable age control points: one after the mid-Miocene, one around the early Tortonian period, and one before the early Pliocene. By comparing the climate states in the middle and late Miocene, the precipitation changes can be categorized into three states: dry, wet, and unchanged. In the absence of direct comparisons between the two periods, we selected near locations, with most comparable points having an average latitude and longitude deviation of within 1.5°. For sampling points lacking latitude and longitude coordinates in the original study, we verified their locations via Google Maps.

Models

CESM 1.2.2, developed at the National Center for Atmospheric Research, consists of atmosphere, land, sea ice, ocean, and river systems (*56*). The Community Atmosphere Model version 4 (CAM4) is used here as the atmospheric component and runs with a finite-volume dynamical core (*57*). The land component, Community Land Model version 4 (CLM4), includes processes associated with snow, water storage, vegetation, etc. (*58*). All simulations are run with the f19_g16 configuration, in which CAM4 and CLM4 have a horizontal resolution of ~1.9° (latitude) × 2.5° (longitude), and the ocean component (Parallel Ocean Program ocean model version 2) (*59*) and sea ice component (Community Ice CodE version 4.0) (*60*) have a horizontal resolution of ~1° (384 × 320 grid points in the meridional and zonal directions, respectively). The atmosphere and ocean components have 26 and 60 layers in the vertical direction, respectively. In CLM4, multiple land surface types and plant functional types are contained within one grid, and CLM4 can be run in the prognostic carbon–nitrogen (CN) model with dynamic vegetation (CNDV) to simulate natural vegetation. However, owing to the simulated biases of CNDV (*61*), we use BIOME4 (*62*) to simulate the vegetation adapted to the climate.

BIOME4 is an equilibrium biogeography model (*62*) that is widely used in simulations of equilibrated vegetation in past and future climate projections (*63*). It simulates 28 biomes at a horizontal resolution of 0.5° latitude by 0.5° longitude and uses the different bioclimatic limits (temperature resistance, moisture requirements, and sunshine amount) among plant functional types to simulate the potential natural vegetation of a given climate.

Experimental design

For the boundary conditions, we use middle Miocene (~14 Ma) and late Miocene (~6 Ma) paleogeographies (fig. S5) (*34*), which use a published plate kinematic model, oceanic lithospheric paleo-ages, and oceanic sediment thicknesses and incorporate global fossil records, stratigraphy, lithofacies, paleoenvironment, and paleoelevation data. Moreover, we use the modified paleovegetation from the proxy-based reconstruction of the Tortonian (*64*) with full ice cover in Antarctica for the late Miocene and the same paleovegetation but less ice cover in Antarctica for the middle Miocene according to the reconstruction for the middle Miocene (*65*). Except for paleogeography, vegetation/ice sheets, and atmospheric CO_2, we keep the

other boundary conditions unchanged, such as the solar constant (1365 W/m^2), preindustrial atmospheric CH_4 and N_2O (760 and 270 parts per billion by volume, respectively), zero concentration of chlorofluorocarbons, and modern orbital parameters (1950 CE).

We conduct seven experiments in total (Table 1). According to the atmospheric CO_2 concentration during the middle Miocene (*21*, *66*), the MM700 experiment was conducted with middle Miocene paleogeography (*34*), vegetation/ice sheet (*64*, *65*), and an atmospheric CO_2 concentration of 700 parts per million by volume (ppmv). Experiment MM280 has the same settings as experiment MM700, except for a low atmospheric CO_2 concentration (280 ppmv), according to the level of atmospheric CO_2 concentration during the late Miocene (*21*, *66*). In comparison, the LM280 experiment is conducted with late Miocene paleogeography (*34*), vegetation/ice sheet (*64*), and an atmospheric CO_2 concentration of 280 ppmv. With these three experiments, which use the same prescribed vegetation, we can compare the effects of paleogeography and the atmospheric CO_2 concentration on climate change. To further evaluate the effects of topographic changes, one more experiment (MM280_LMtopo) is conducted under the boundary conditions from MM280, but the topography and ice sheet are replaced with conditions from LM280.

Three additional experiments (MM700veg, MM280veg, and LM280veg) are conducted to simulate how the vegetation changes as a result of the paleogeographic and atmospheric CO_2 constraints and to investigate the corresponding climate effects of those changes. These experiments apply the same settings as the MM700, MM280, and LM280 experiments, except for the use of dynamic vegetation through asymmetric coupling between CESM and BIOME4 to consider interactions between vegetation and climate. Specifically, monthly precipitation, temperature, and percent sunshine data from the last 10 years of simulation by the CESM and atmospheric CO_2 concentration are used as input parameters in BIOME4 to obtain the distributions of 28 biomes. The simulated vegetation distribution is then used to create surface data to force the next 40 years of simulation of the CESM. Coupling between CESM and BIOME4 is performed every 40 years until the simulations reach the quasi-equilibrium status.

The MM700, MM280, and LM280 experiments are initialized from a static ocean that uses Levitus temperature and salinity profiles and run for 2200 or 2500 model years. Experiment MM280_LMtopo is initialized from the end of experiment MM280 and runs for 500 model years. The MM700veg, MM280veg, and LM280veg experiments are initialized from the end of the MM700, MM280, and LM280 experiments, respectively, and run for 600 model years. From the temporal evolution of the annual global mean SAT and top of the atmosphere (TOA) radiation imbalance in each experiment (fig. S14), all experiments have reached quasi-equilibrium status. In particular, the TOA radiation imbalance averaged over the last 100 model years is less than 0.1 W m^{-2}, and the global mean SAT trend is less than 0.1°C per century (Table 1). Thus, we focus on analyzing the climatological means of the last 100 model years in each experiment above.

The effects of combined paleogeographic change and atmospheric CO_2 decline with static prescribed vegetation: LM280 − MM700. The effect of atmospheric CO_2 decline with static prescribed vegetation: MM280 − MM700. The effect of paleogeographic change with static prescribed vegetation: LM280 − MM280. The effect of vegetation feedbacks from changes in both paleogeography and atmospheric CO_2: (LM280veg − MM700veg) − (LM280 − MM700). The effect of vegetation feedbacks from atmospheric CO_2 decline: (MM280veg − MM700veg) − (MM280 − MM700). The effect of vegetation feedbacks from paleogeographic change: (LM280veg − MM280veg) − (LM280 − MM280).

Analysis

Energy components for temperature

The surface NR (Q_N) is a budget composed of ISR (Q_{IS}), RSR (Q_{RS}) that depends on the land surface albedo (α), DLR (Q_{DL}), and longwave radiation emitted from the land surface (Q_{EL})

$$Q_N = Q_{IS} - Q_{RS} + Q_{DL} - Q_{EL} \quad (1)$$

$$= Q_{IS}(1-\alpha) + Q_{DL} - Q_{EL} \quad (2)$$

The available NR is used for the phase change of water in the form of latent heat (*LE*), changing the air temperature in the form of sensible heat (*SH*), and subsurface heat in the form of ground heat (*GH*)

$$Q_N = SH + LE + GH \quad (3)$$

In accordance with the Stefan-Boltzmann law, the surface temperature is determined by the radiation emitted by the land surface

$$\sigma T^4 = Q_{EL} = Q_{IS}(1-\alpha) + Q_{DL} - (SH + LE + GH) \quad (4)$$

Therefore, surface temperature is determined by the budgets of ISR, albedo, DLR, and sensible, latent, and ground heat fluxes.

Moisture budget analysis

The moisture budget analysis was performed following previously reported methods (*67*). The following equation is commonly used to estimate changes in precipitation

$$\begin{aligned} P' &\approx E' - \langle \nabla \cdot vq \rangle' + \delta \\ &\approx E' - \langle q \nabla \cdot v \rangle' - \langle v \cdot \nabla q \rangle' \end{aligned} \quad (5)$$

P represents precipitation; *E* represents evaporation; *v* represents horizontal velocity; *q* represents specific humidity; ′ represents the difference between two experiments; and ⟨ ⟩ represents the column integration from the surface to 100 hPa. The residual term δ includes transient eddies and nonlinear effects and is relatively small and neglected here.

With the assumption that the pressure velocity ω is zero at the surface and at tropopause, the above equation can be rewritten as

$$P' \approx E' - \left\langle \omega \partial_p q \right\rangle' - \langle v \cdot \nabla q \rangle' \quad (6)$$

Both vertical moisture advection $\left(-\left\langle \omega \partial_p q \right\rangle'\right)$ and horizontal moisture advection $(-\langle v \cdot \nabla q \rangle')$ can be divided into thermodynamic and dynamic components, and the moisture budget equation has the following reformed equation

$$P' \approx E' - \left\langle \overline{\omega} \partial_p q' \right\rangle - \left\langle \omega' \partial_p \overline{q} \right\rangle - \left\langle \overline{v} \cdot \nabla q' \right\rangle - \left\langle v' \cdot \nabla \overline{q} \right\rangle \quad (7)$$

The terms $-\left\langle \overline{\omega} \partial_p q' \right\rangle$ and $-\left\langle \omega' \partial_p \overline{q} \right\rangle$ are related to the thermodynamic and dynamic components of vertical moisture advection, respectively. The terms $-\langle \overline{v} \cdot \nabla q' \rangle$ and $-\langle v' \cdot \nabla \overline{q} \rangle$ are related to the thermodynamic and dynamic components of horizontal moisture advection, respectively.

Supplementary Materials

The PDF file includes:
Figs. S1 to S14
Legends for tables S1 to S3
References

Other Supplementary Material for this manuscript includes the following:
Tables S1 to S3

REFERENCES AND NOTES

1. T. D. Herbert, K. T. Lawrence, A. Tzanova, L. C. Peterson, R. Caballero-Gill, C. S. Kelly, Late Miocene global cooling and the rise of modern ecosystems. *Nat. Geosci.* **9**, 843–847 (2016).
2. T. Westerhold, N. Marwan, A. J. Drury, D. Liebrand, C. Agnini, E. Anagnostou, J. S. K. Barnet, S. M. Bohaty, D. De Vleeschouwer, F. Florindo, T. Frederichs, D. A. Hodell, A. E. Holbourn, D. Kroon, V. Lauretano, K. Littler, L. J. Lourens, M. Lyle, H. Palike, U. Rohl, J. Tian, R. H. Wilkens, P. A. Wilson, J. C. Zachos, An astronomically dated record of Earth's climate and its predictability over the last 66 million years. *Science* **369**, 1383–1387 (2020).
3. M. Steinthorsdottir, H. K. Coxall, A. M. de Boer, M. Huber, N. Barbolini, C. D. Bradshaw, N. J. Burls, S. J. Feakins, E. Gasson, J. Henderiks, A. E. Holbourn, S. Kiel, M. J. Kohn, G. Knorr, W. M. Kurschner, C. H. Lear, D. Liebrand, D. J. Lunt, T. Mors, P. N. Pearson, M. J. Pound, H. Stoll, C. A. E. Stromberg, The Miocene: The future of the past. *Paleoceanogr. Paleoclimatol.* **36**, e2020PA004037 (2021).
4. Y. F. Miao, X. M. Fang, J. M. Sun, W. J. Xiao, Y. H. Yang, X. L. Wang, A. Farnsworth, K. Y. Huang, Y. L. Ren, F. L. Wu, Q. Q. Qiao, W. L. Zhang, Q. Q. Meng, X. L. Yan, Z. Zheng, C. H. Song, T. Utescher, A new biologic paleoaltimetry indicating late Miocene rapid uplift of northern Tibet Plateau. *Science* **378**, 1074–1078 (2022).
5. J. Sun, Z. L. Ding, W. J. Xiao, B. F. Windley, Coupling between uplift of the central Asian orogenic belt-NE Tibetan Plateau and accumulation of aeolian red clay in the inner Asia began at ~7 Ma. *Earth Sci. Rev.* **226**, 103919 (2022).
6. X. M. Fang, M. D. Yan, R. Van der Voo, D. K. Rea, C. H. Song, J. M. Pares, J. P. Gao, J. Nie, S. Dai, Late Cenozoic deformation and uplift of the NE Tibetan Plateau: Evidence from high-resolution magnetostratigraphy of the Guide Basin, Qinghai Province, China. *Geol. Soc. Am. Bull.* **117**, 1208–1225 (2005).
7. K. E. Karlstrom, D. Coblentz, K. Dueker, W. Ouimet, E. Kirby, J. Van Wijk, B. Schmandt, S. Kelley, G. Lazear, L. J. Crossey, R. Crow, A. Aslan, A. Darling, R. Aster, J. MacCarthy, S. M. Hansen, J. Stachnik, D. F. Stockli, R. V. Garcia, M. Hoffman, R. McKeon, J. Feldman, M. Heizler, M. S. Donahue, C. W. Grp, Mantle-driven dynamic uplift of the Rocky Mountains and Colorado Plateau and its surface response: Toward a unified hypothesis. *Lithosphere* **4**, 3–22 (2012).
8. K. M. Gregory-Wodzicki, Uplift history of the central and northern Andes: A review. *GSA Bull.* **112**, 1091–1105 (2000).
9. P. Sepulchre, G. Ramstein, F. Fluteau, M. Schuster, J.-J. Tiercelin, M. Brunet, Tectonic uplift and eastern Africa aridification. *Science* **313**, 1419–1423 (2006).
10. A. J. Vernon, P. A. van der Beek, H. D. Sinclair, M. K. Rahn, Increase in late Neogene denudation of the European Alps confirmed by analysis of a fission-track thermochronology database. *Earth Planet. Sci. Lett.* **270**, 316–329 (2008).
11. C. Badgley, J. C. Barry, M. E. Morgan, S. V. Nelson, A. K. Behrensmeyer, T. E. Cerling, D. Pilbeam, Ecological changes in Miocene mammalian record show impact of prolonged climatic forcing. *Proc. Natl. Acad. Sci. U.S.A.* **105**, 12145–12149 (2008).
12. H. L. Wang, H. Y. Lu, Climate controls on evolution of grassland ecosystems since late Cenozoic: A phytolith perspective. *Earth Sci. Rev.* **231**, 104059 (2022).
13. C. P. Chamberlain, M. J. Winnick, H. T. Mix, S. D. Chamberlain, K. Maher, The impact of neogene grassland expansion and aridification on the isotopic composition of continental precipitation. *Global Biogeochem. Cycles* **28**, 992–1004 (2014).
14. G. M. Semprebon, F. Rivals, C. M. Janis, The role of grass vs. exogenous abrasives in the paleodietary patterns of North American ungulates. *Front. Ecol. Evol.* **7**, 65 (2019).
15. Y. Suganuma, T. Hamada, S. Tanaka, M. Okada, H. Nakaya, Y. Kunimatsu, H. Saegusa, S. Nagaoka, B. Ratanasthien, Magnetostratigraphy of the Miocene Chiang Muan formation, northern Thailand: Implication for revised chronology of the earliest Miocene hominoid in Southeast Asia. *Paleogeogr. Paleoclimatol. Paleoecol.* **239**, 75–86 (2006).
16. P. G. DeCelles, G. E. Gehrels, J. Quade, T. P. Ojha, P. A. Kapp, B. N. Upreti, Neogene foreland basin deposits, erosional unroofing, and the kinematic history of the Himalayan fold-thrust belt, western Nepal. *Geol. Soc. Am. Bull.* **110**, 2–21 (1998).
17. L. Diester-Haass, P. A. Meyers, T. Bickert, Carbonate crash and biogenic bloom in the late Miocene: Evidence from ODP sites 1085, 1086, and 1087 in the Cape Basin, southeast Atlantic Ocean. *Paleoceanography* **19**, doi:10.1029/2003PA000933 (2004).
18. J. R. Thomson, P. B. Holden, P. Anand, N. R. Edwards, C. A. Porchier, N. B. W. Harris, Tectonic and climatic drivers of Asian monsoon evolution. *Nat. Commun.* **12**, 4022 (2021).
19. A. Farnsworth, D. J. Lunt, S. A. Robinson, P. J. Valdes, W. H. G. Roberts, P. D. Clift, P. Markwick, T. Su, N. Wrobel, F. Bragg, S. J. Kelland, R. D. Pancost, Past East Asian monsoon evolution controlled by paleogeography, not CO_2. *Sci. Adv.* **5**, eaax1697 (2019).
20. D. Tardif, A. C. Sarr, F. Fluteau, A. Licht, M. Kaya, J. B. Ladant, N. Meijer, Y. Donnadieu, G. Dupont-Nivet, C. T. Bolton, G. Le Hir, Q. Pillot, F. Poblete, P. Sepulchre, A. Toumoulin, W. Banfield, The role of paleogeography in Asian monsoon evolution: A review and new insights from climate modelling. *Earth Sci. Rev.* **243**, 104464 (2023).
21. R. M. Brown, T. B. Chalk, A. J. Crocker, P. A. Wilson, G. L. Foster, Late Miocene cooling coupled to carbon dioxide with Pleistocene-like climate sensitivity. *Nat. Geosci.* **15**, 664–670 (2022).
22. H. Zhang, H. Lu, J. He, W. Xie, H. Wang, H. Zhang, D. Breecker, A. Bird, T. Stevens, J. Nie, G. Li, Large-number detrital zircon U-Pb ages reveal global cooling caused the formation of the Chinese Loess Plateau during late Miocene. *Sci. Adv.* **8**, eabq2007 (2022).
23. Y. F. Miao, M. Herrmann, F. Wu, X. Yan, S. Yang, What controlled mid–late Miocene long-term aridification in central Asia?—Global cooling or Tibetan Plateau uplift: A review. *Earth Sci. Rev.* **112**, 155–172 (2012).
24. R. Feng, T. Bhattacharya, B. L. Otto-Bliesner, E. C. Brady, A. M. Haywood, J. C. Tindall, S. J. Hunter, A. Abe-Ouchi, W. L. Chan, M. Kageyama, C. Contoux, C. Guo, X. Li, G. Lohmann, C. Stepanek, N. Tan, Q. Zhang, Z. Zhang, Z. Han, C. J. R. Williams, D. J. Lunt, H. J. Dowsett, D. Chandan, W. R. Peltier, Past terrestrial hydroclimate sensitivity controlled by Earth system feedbacks. *Nat. Commun.* **13**, 1306 (2022).
25. C. D. Bradshaw, D. J. Lunt, R. Flecker, T. Davies-Barnard, Disentangling the roles of late Miocene palaeogeography and vegetation—Implications for climate sensitivity. *Paleogeogr. Paleoclimatol. Paleoecol.* **417**, 17–34 (2015).
26. G. Lohmann, M. Butzin, T. Bickert, V. Mosbrugger, Effect of vegetation on the late Miocene ocean circulation. *J. Mar. Sci. Eng.* **3**, 1311–1333 (2015).
27. G. Knorr, M. Butzin, A. Micheels, G. Lohmann, A warm Miocene climate at low atmospheric CO_2 levels. *Geophys. Res. Lett.* **38**, doi:10.1029/2011GL048873 (2011).
28. P. J. Polissar, C. Rose, K. T. Uno, S. R. Phelps, P. deMenocal, Synchronous rise of African C_4 ecosystems 10 million years ago in the absence of aridification. *Nat. Geosci.* **12**, 657–660 (2019).
29. B. Carrapa, M. Clementz, R. Feng, Ecological and hydroclimate responses to strengthening of the Hadley circulation in South America during the late Miocene cooling. *Proc. Natl. Acad. Sci. U.S.A.* **116**, 9747–9752 (2019).
30. D. L. Fox, J. G. Honey, R. A. Martin, P. Pelaez-Campomanes, Pedogenic carbonate stable isotope record of environmental change during the Neogene in the southern Great Plains, southwest Kansas, USA: Carbon isotopes and the evolution of C_4-dominated grasslands. *Geol. Soc. Am. Bull.* **124**, 444–462 (2012).
31. B. H. Passey, L. K. Ayliffe, A. Kaakinen, Z. Q. Zhang, J. T. Eronen, Y. M. Zhu, L. P. Zhou, T. E. Cerling, M. Fortelius, Strengthened East Asian summer monsoons during a period of high-latitude warmth? Isotopic evidence from Mio-Pliocene fossil mammals and soil carbonates from northern China. *Earth Planet. Sci. Lett.* **277**, 443–452 (2009).
32. M. J. Pound, A. M. Haywood, U. Salzmann, J. B. Riding, Global vegetation dynamics and latitudinal temperature gradients during the mid to late Miocene (15.97-5.33 Ma). *Earth Sci. Rev.* **112**, 1–22 (2012).
33. J. Zhang, X. Q. Li, H. W. Peng, L. S. Hai, A. S. Erst, F. Jabbour, R. D. Ortiz, F. C. Xia, P. S. Soltis, D. E. Soltis, W. Wang, Evolutionary history of the Arctic flora. *Nat. Commun.* **14**, 4021 (2023).
34. Z. L. He, Z. S. Zhang, Z. T. Guo, C. R. Scotese, C. L. Deng, Middle Miocene (~14 Ma) and late Miocene (~6 Ma) paleogeographic boundary conditions. *Paleoceanogr. Paleoclimatol.* **36**, e2021PA004298 (2021).
35. N. J. Burls, C. D. Bradshaw, A. M. De Boer, N. Herold, M. Huber, M. Pound, Y. Donnadieu, A. Farnsworth, A. Frigola, E. Gasson, A. S. von der Heydt, D. K. Hutchinson, G. Knorr, K. T. Lawrence, C. H. Lear, X. Li, G. Lohmann, D. J. Lunt, A. Marzocchi, M. Prange, C. A. Riihimaki, A. C. Sarr, N. Siler, Z. Zhang, Simulating Miocene warmth: Insights from an opportunistic multi-model ensemble (MioMIP1). *Paleoceanogr. Paleoclimatol.* **36**, e2020PA004054 (2021).
36. J. W. B. Rae, Y. G. Zhang, X. Q. Liu, G. L. Foster, H. M. Stoll, R. D. M. Whiteford, Atmospheric CO_2 over the past 66 million years from marine archives. *Annu. Rev. Earth Planet. Sci.* **49**, 609–641 (2021).
37. B. Hönisch, D. L. Royer, D. O. Breecker, P. J. Polissar, G. J. Bowen, M. J. Henehan, Y. Cui, M. Steinthorsdottir, J. C. McElwain, M. J. Kohn, A. Pearson, S. R. Phelps, K. T. Uno, A. Ridgwell, E. Anagnostou, J. Austermann, M. P. S. Badger, R. S. Barclay, P. K. Bijl, T. B. Chalk, C. R. Scotese, E. de la Vega, R. M. DeConto, K. A. Dyez, V. Ferrini, P. J. Franks, C. F. Giulivi, M. Gutjahr, D. T. Harper, L. L. Haynes, M. Huber, K. E. Snell, B. A. Keisling, W. Konrad, T. K. Lowenstein, A. Malinverno, M. Guillermic, L. M. Mejía, J. N. Milligan, J. J. Morton, L. Nordt, R. Whiteford, A. Roth-Nebelsick, J. K. C. Rugenstein, M. F. Schaller, N. D. Sheldon, S. Sosdian, E. B. Wilkes, C. R. Witkowski, Y. G. Zhang, L. Anderson, D. J. Beerling, C. Bolton, T. E. Cerling, J. M. Cotton, J. Da, D. D. Ekart, G. L. Foster, D. R. Greenwood, E. G. Hyland, E. A. Jagniecki, J. P. Jasper, J. B. Kowalczyk, L. Kunzmann, W. M. Kürschner, C. E. Lawrence, C. H. Lear, M. A. Martínez-Botí, D. P. Maxbauer, P. Montagna, B. D. A. Naafs, J. W. B. Rae, M. Raitzsch, G. J. Retallack, S. J. Ring, O. Seki, J. Sepúlveda, A. Sinha, T. F. Tesfamichael, A. Tripati, J. van der Burgh, J. Yu, J. C. Zachos, L. Zhang, Toward a Cenozoic history of atmospheric CO_2. *Science* **382**, eadi5177 (2023).

38. J. M. Wallace, P. V. Hobbs, Atmospheric Science: An Introductory Survey (Academic Press, ed. 2, 2006).
39. C. A. E. Strömberg, Evolution of grasses and grassland ecosystems. *Annu. Rev. Earth Planet. Sci.* **39**, 517–544 (2011).
40. N. Barbolini, A. Woutersen, G. Dupont-Nivet, D. Silvestro, D. Tardif, P. M. C. Coster, N. Meijer, C. Chang, H. X. Zhang, A. Licht, C. Rydin, A. Koutsodendris, F. Han, A. Rohrmann, X. J. Liu, Y. Zhang, Y. Donnadieu, F. Fluteau, J. B. Ladant, G. Le Hir, C. Hoorn, Cenozoic evolution of the steppe-desert biome in Central Asia. *Sci. Adv.* **6**, eabb8227 (2020).
41. R. Bonnefille, Cenozoic vegetation, climate changes and hominid evolution in tropical Africa. *Glob. Planet. Change* **72**, 390–411 (2010).
42. H. A. Martin, Cenozoic climatic change and the development of the arid vegetation in Australia. *J. Arid Environ.* **66**, 533–563 (2006).
43. Z. Zhang, G. Ramstein, M. Schuster, C. Li, C. Contoux, Q. Yan, Aridification of the Sahara desert caused by Tethys Sea shrinkage during the late Miocene. *Nature* **513**, 401–404 (2014).
44. J. Sun, Z. Zhang, L. Zhang, New evidence on the age of the Taklimakan Desert. *Geology* **37**, 159–162 (2009).
45. Z. Q. Yao, X. F. Shi, Z. T. Guo, X. Z. Li, B. N. Nath, C. Betzler, H. Zhang, S. Lindhorst, P. Miriyala, Weakening of the South Asian summer monsoon linked to interhemispheric ice-sheet growth since 12 Ma. *Nat. Commun.* **14**, 829 (2023).
46. D. Ferreira, P. Cessi, H. K. Coxall, A. de Boer, H. A. Dijkstra, S. S. Drijfhout, T. Eldevik, N. Harnik, J. F. McManus, D. P. Marshall, J. Nilsson, F. Roquet, T. Schneider, R. C. Wills, Atlantic-Pacific asymmetry in deep water formation. *Annu. Rev. Earth Planet. Sci.* **46**, 327–352 (2018).
47. V. Kirillova, A. H. Osborne, T. Störling, M. Frank, Miocene restriction of the Pacific-North Atlantic throughflow strengthened Atlantic overturning circulation. *Nat. Commun.* **10**, 4025 (2019).
48. N. Herold, M. Huber, R. Müller, M. Seton, Modeling the Miocene climatic optimum: Ocean circulation. *Paleoceanography* **27**, PA1209 (2012).
49. C. M. Brierley, A. V. Fedorov, Comparing the impacts of Miocene-Pliocene changes in inter-ocean gateways on climate: Central American Seaway, Bering Strait, and Indonesia. *Earth Planet. Sci. Lett.* **444**, 116–130 (2016).
50. N. Tan, Z. S. Zhang, Z. T. Guo, C. C. Guo, Z. J. Zhang, Z. L. He, G. Ramstein, Recognizing the role of tropical seaways in modulating the Pacific circulation. *Geophys. Res. Lett.* **49**, e2022GL099674 (2022).
51. T. Utescher, D. Djordjevic-Milutinovic, A. Bruch, V. Mosbrugger, Palaeoclimate and vegetation change in Serbia during the last 30 Ma. *Paleogeogr. Paleoclimatol. Paleoecol.* **253**, 141–152 (2007).
52. D. Ivanov, A. R. Ashraf, V. Mosbrugger, E. Palamarev, Palynological evidence for Miocene climate change in the Forecarpathian Basin (Central Paratethys, NW Bulgaria). *Paleogeogr. Paleoclimatol. Paleoecol.* **178**, 19–37 (2002).
53. T. Utescher, A. A. Bruch, B. Erdei, L. François, D. Ivanov, F. M. B. Jacques, A. K. Kern, Y. S. Liu, V. Mosbrugger, R. A. Spicer, The coexistence approach—Theoretical background and practical considerations of using plant fossils for climate quantification. *Paleogeogr. Paleoclimatol. Paleoecol.* **410**, 58–73 (2014).
54. C. A. Metzger, G. J. Retallack, Paleosol record of Neogene climate change in the Australian outback. *Aust. J. Earth Sci.* **57**, 871–885 (2010).
55. G. J. Retallack, Mallee model for mammal communities of the early Cenozoic and Mesozoic. *Paleogeogr. Paleoclimatol. Paleoecol.* **342-343**, 111–129 (2012).
56. J. W. Hurrell, M. M. Holland, P. R. Gent, S. Ghan, J. E. Kay, P. J. Kushner, J. F. Lamarque, W. G. Large, D. Lawrence, K. Lindsay, W. H. Lipscomb, M. C. Long, N. Mahowald, D. R. Marsh, R. B. Neale, P. Rasch, S. Vavrus, M. Vertenstein, D. Bader, W. D. Collins, J. J. Hack, J. Kiehl, S. Marshall, The Community Earth System Model: A framework for collaborative research. *Bull. Amer. Meteorol. Soc.* **94**, 1339–1360 (2013).
57. R. B. Neale, J. Richter, S. Park, P. H. Lauritzen, S. J. Vavrus, P. J. Rasch, M. Zhang, The mean climate of the Community Atmosphere Model (CAM4) in forced SST and fully coupled experiments. *J. Climate* **26**, 5150–5168 (2013).
58. D. M. Lawrence, K. W. Oleson, M. G. Flanner, P. E. Thornton, S. C. Swenson, P. J. Lawrence, X. B. Zeng, Z. L. Yang, S. Levis, K. Sakaguchi, G. B. Bonan, A. G. Slater, Parameterization improvements and functional and structural advances in version 4 of the Community Land Model. *J. Adv. Model. Earth Syst.* **3**, M03001 (2011).
59. R. Smith, P. Jones, B. Briegleb, F. Bryan, G. Danabasoglu, J. Dennis, J. Dukowicz, The Parallel Ocean Program (POP) reference manual ocean component of the Community Climate System Model (CCSM) and Community Earth System Model (CESM). *LAUR-10-01853* **141**, 1–140 (2010).
60. E. C. Hunke, W. H. Lipscomb, A. K. Turner, N. Jeffery, S. Elliott, CICE: The Los Alamos Sea Ice model documentation and software user's manual version 4.1. Fluid Dynamics Group, Los Alamos National Laboratory 675, 500 (2010).
61. C. K. G. Castillo, S. Levis, P. Thornton, Evaluation of the new CNDV option of the Community Land Model: Effects of dynamic vegetation and interactive nitrogen on CLM4 means and variability. *J. Climate* **25**, 3702–3714 (2012).
62. J. O. Kaplan, N. H. Bigelow, I. C. Prentice, S. P. Harrison, P. J. Bartlein, T. R. Christensen, W. Cramer, N. V. Matveyeva, A. D. McGuire, D. F. Murray, V. Y. Razzhivin, B. Smith, D. A. Walker, P. M. Anderson, A. A. Andreev, L. B. Brubaker, M. E. Edwards, A. V. Lozhkin, Climate change and Arctic ecosystems: 2. Modeling, paleodata-model comparisons, and future projections. *J. Geophys. Res.-Atmos.* **108**, doi:10.1029/2002JD002559 (2003).
63. U. Salzmann, A. M. Haywood, D. J. Lunt, The past is a guide to the future? Comparing middle Pliocene vegetation with predicted biome distributions for the twenty-first century. *Philos. Trans. R. Soc. A-Math. Phys. Eng. Sci.* **367**, 189–204 (2009).
64. A. Micheels, A. A. Bruch, D. Uhl, T. Utescher, V. Mosbrugger, A late Miocene climate model simulation with ECHAM4/ML and its quantitative validation with terrestrial proxy data. *Paleogeogr. Paleoclimatol. Paleoecol.* **253**, 251–270 (2007).
65. A. Frigola, M. Prange, M. Schulz, Boundary conditions for the Middle Miocene Climate Transition (MMCT v1.0). *Geosci. Model Dev.* **11**, 1607–1626 (2018).
66. T. D. Herbert, C. A. Dalton, Z. H. Liu, A. Salazar, W. M. Si, D. S. Wilson, Tectonic degassing drove global temperature trends since 20 Ma. *Science* **377**, 116–119 (2022).
67. C. Chou, J. C. H. Chiang, C. W. Lan, C. H. Chung, Y. C. Liao, C. J. Lee, Increase in the range between wet and dry season precipitation. *Nat. Geosci.* **6**, 263–267 (2013).
68. J. A. Kirschner, C. Hoorn, The onset of grasses in the Amazon drainage basin, evidence from the fossil record. *Front. Biogeogr.* **12**, e44827 (2020).
69. Y. F. Miao, X. M. Fang, M. Herrmann, F. L. Wu, Y. Z. Zhang, D. L. Liu, Miocene pollen record of KC-1 core in the Qaidam Basin, NE Tibetan Plateau and implications for evolution of the East Asian monsoon. *Paleogeogr. Paleoclimatol. Paleoecol.* **299**, 30–38 (2011).
70. B. J. Tipple, M. Pagani, A 35 Myr North American leaf-wax compound-specific carbon and hydrogen isotope record: Implications for C_4 grasslands and hydrologic cycle dynamics. *Earth Planet. Sci. Lett.* **299**, 250–262 (2010).
71. T. E. Cerling, J. M. Harris, B. J. MacFadden, M. G. Leakey, J. Quade, V. Eisenmann, J. R. Ehleringer, Global vegetation change through the Miocene/Pliocene boundary. *Nature* **389**, 153–158 (1997).
72. P. D. Clift, K. V. Hodges, D. Heslop, R. Hannigan, H. Van Long, G. Calves, Correlation of Himalayan exhumation rates and Asian monsoon intensity. *Nat. Geosci.* **1**, 875–880 (2008).
73. Y. Jia, H. B. Wu, W. C. Zhang, Q. Li, Y. Y. Yu, C. X. Zhang, A. Z. Sun, Quantitative Cenozoic climatic reconstruction and its implications for aridification of the northeastern Tibetan Plateau. *Paleogeogr. Paleoclimatol. Paleoecol.* **567**, 110244 (2021).
74. S. Syabryaj, T. Utescher, S. Molchanoff, A. A. Bruch, Vegetation and palaeoclimate in the Miocene of Ukraine. *Paleogeogr. Paleoclimatol. Paleoecol.* **253**, 153–168 (2007).
75. M. E. Gibson, J. McCoy, J. M. K. O'Keefe, N. B. N. Otaño, S. Warny, M. J. Pound, Reconstructing terrestrial paleoclimates: A comparison of the co-existence approach, Bayesian and probability reconstruction techniques using the UK Neogene. *Paleoceanogr. Paleoclimatology* **37**, e2021PA004358 (2022).
76. R. D. Müller, S. Zahirovic, S. E. Williams, J. Cannon, M. Seton, D. J. Bower, M. G. Tetley, C. Heine, E. Le Breton, S. F. Liu, S. H. J. Russell, T. Yang, J. Leonard, M. Gurnis, A global plate model including lithospheric deformation along major rifts and orogens since the Triassic. *Tectonics* **38**, 1884–1907 (2019).
77. J. M. Cotton, E. G. Hyland, N. D. Sheldon, Multi-proxy evidence for tectonic control on the expansion of C_4 grasses in northwest Argentina. *Earth Planet. Sci. Lett.* **395**, 41–50 (2014).
78. S. T. Chen, S. Y. Smith, N. D. Sheldon, C. A. E. Strömberg, Regional-scale variability in the spread of grasslands in the late Miocene. *Paleogeogr. Paleoclimatol. Paleoecol.* **437**, 42–52 (2015).
79. E. G. Hyland, N. D. Sheldon, S. Y. Smith, C. A. E. Strömberg, Late Miocene rise and fall of C_4 grasses in the western United States linked to aridification and uplift. *Geol. Soc. Am. Bull.* **131**, 224–234 (2019).
80. G. Srivastava, K. N. Paudayal, T. Utescher, R. C. Mehrotra, Miocene vegetation shift and climate change: Evidence from the Siwalik of Nepal. *Glob. Planet. Change* **161**, 108–120 (2018).
81. S. F. Li, P. J. Valdes, A. Farnsworth, T. Davies-Barnard, T. Su, D. J. Lunt, R. A. Spicer, J. Liu, W. Y. D. Deng, J. Huang, H. Tang, A. Ridgwell, L. L. Chen, Z. K. Zhou, Orographic evolution of northern Tibet shaped vegetation and plant diversity in eastern Asia. *Sci. Adv.* **7**, eabc7741 (2021).
82. B. Wang, J. Liu, H. J. Kim, P. J. Webster, S. Y. Yim, Recent change of the global monsoon precipitation (1979–2008). *Climate Dynam.* **39**, 1123–1135 (2012).
83. P. Braconnot, B. Otto-Bliesner, S. Harrison, S. Joussaume, J. Y. Peterchmitt, A. Abe-Ouchi, M. Crucifix, E. Driesschaert, T. Fichefet, C. D. Hewitt, M. Kageyama, A. Kitoh, M. F. Loutre, O. Marti, U. Merkel, G. Ramstein, P. Valdes, L. Weber, Y. Yu, Y. Zhao, Results of PMIP2 coupled simulations of the mid-Holocene and Last Glacial Maximum - Part 2: Feedbacks with emphasis on the location of the ITCZ and mid- and high latitudes heat budget. *Clim. Past* **3**, 279–296 (2007).

Acknowledgments: We thank the National Large Scientific and Technological Infrastructure "Earth System Numerical Simulation Facility" (https://cstr.cn/31134.02.EL) for the technical support. **Funding:** This study was supported by the National Key R&D Program of China (2023YFF0803500 to R.Z. and J.S.), the Western Light Project of Chinese Academy of Sciences

(xbzg-zdsys-202204 to R.Z.), the National Natural Science Foundation of China (42488201 to J.S., 42371166 and 42071113 to R.Z., and 42372033 to S.L.), and the Young and Middle-aged Academic and Technical Leaders of Yunnan (202305AC160051 to S.L.). **Author contributions:** Conceptualization: R.Z. and J.S. Methodology: R.Z., J.G., T.S., S.L., and J.Z. Investigation: R.Z., C.D.B., X.X., and X.L. Visualization: R.Z., T.S., J.Z., S.L., and Z.L. Supervision: R.Z. and J.S. Writing—original draft: R.Z. and T.S. Writing—review and editing: All authors. **Competing interests:** The authors declare that they have no competing interests. **Data and materials availability:** The model results are archived at https://zenodo.org/records/14175658. All data needed to evaluate the conclusions in the paper are present in the paper and/or the Supplementary Materials.

Submitted 23 August 2024
Accepted 27 March 2025
Published 2 May 2025
10.1126/sciadv.ads4268